



Experimental and computational assessment of minimizing overfill in trajectory corners by laser velocity control of laser cladding

Diego Montoya-Zapata^{1,2} · Jorge Posada¹ · Piera Alvarez³ · Carles Creus¹ · Aitor Moreno¹ · Igor Ortiz³ · Oscar Ruiz-Salguero²

Received: 5 August 2021 / Accepted: 27 December 2021
© The Author(s), under exclusive licence to Springer-Verlag London Ltd., part of Springer Nature 2022

Abstract

In the context of laser metal deposition (LMD), the problem of avoiding unintentional material accumulation in bead corners or bends is central. Most of the existing approaches to limit such an accumulation are expensive trial-and-error ones. This manuscript presents the experimental verification of a recently reported computational method for minimizing material overfill in corners in LMD. The verification consisted in the deposition of single-layer corners with angle $\theta \in \{15^\circ, 30^\circ, 45^\circ, 60^\circ, 75^\circ\}$ with (i) constant and (ii) controlled (as dictated by the computational minimization) tool-head velocity. The term *controlled velocity* in this manuscript refers to the fact that the nozzle velocity can be adjusted in advance with predefined parameters resulting from the simulations of variable velocities. The comparison between the predicted and experimental bead topographies cannot be executed via standard registration methods because these methods minimize the distance between the registered datasets. In response to this limitation, this manuscript presents a registration method that avoids overall distance minimization. This registration method is based on the sequential matching of datums between the experimental and predicted datasets. The results of the experiments revealed that (i) the computational minimization strategy is effective for reducing material overfill in LMD and (ii) near 40% of the metal powder delivered by the nozzle is wasted. This powder loss is a constant feature across LMD implementations and is not caused by the minimization of metal overfill at corners. These facts show that (i) voxel-based modeling is an effective tool for bead topography and mass/area-based bead computations and (ii) LMD is useful for the cladding stage but not for the production of the bulk piece. Additional work is required to appraise the effective (i.e., not nominal) powder rate deposited at the bead. Future efforts will be dedicated to extend the material overfill minimization strategy to multi-layer deposition.

Keywords Laser metal deposition · Additive manufacturing · Computational optimization · Mesh registration · Physical experiments · Trajectory corners · Bead geometry

Glossary

AM	Additive manufacturing.
CG	Center of gravity.
ICP	Iterative closest point.
LMD	Laser metal deposition.
XCT	X-ray computer tomography.

SO(3)

Special orthogonal group of dimension 3. A matrix \mathbf{R} ($n \times n$) is SO(n) (i.e., is a *rotation*) if $\mathbf{R}^T * \mathbf{R} = \mathbf{R} * \mathbf{R}^T = \mathbf{I}$ and $\det(\mathbf{R}) = +1$.

$\mathbf{C}(u) = [C_x(u), C_y(u)]^T$

Planar parametric curve that represents the tool-path.

$\mathbf{C}^{PL}(\mathbf{c}_0, \dots, \mathbf{c}_N)$

Piecewise linear curve with vertices $\mathbf{c}_k \in \mathbf{C}$, ($k = 0, \dots, N$) that approximates $\mathbf{C}(u)$.

$I(x, y, t) : \mathbb{R}^2 \times \mathbb{R} \rightarrow \mathbb{R}$

Profile of powder delivery [kg/(s mm²)] of a given nozzle at time t . (x, y): local nozzle coordinates.

✉ Aitor Moreno
amoreno@vicomtech.org

¹ Vicomtech Foundation, Basque Research and Technology Alliance (BRTA), Mikeletegi 57, Donostia-San Sebastian 20009, Spain

² Laboratory of CAD CAM CAE, Universidad EAFIT, Cra 49 no 7-sur-50, Medellín 050022, Colombia

³ Ikerlune A.I.E., San Antolin 3, Elgoibar 20870, Spain

$H(x, y, t) : \mathbb{R}^2 \times \mathbb{R} \rightarrow \mathbb{R}$	Bead height [mm] at the point (x, y) of the substrate plate at time t .
$H_0(x, y) : \mathbb{R}^2 \rightarrow \mathbb{R}$	Bead height [mm] at plate point (x, y) under constant nozzle velocity direction and magnitude, and material flow rate.
$H_G^\theta(x, y) : \mathbb{R}^2 \rightarrow \mathbb{R}$	Bead height [mm] of an ideal (or goal) corner with angle θ .
$f(t) : \mathbb{R} \rightarrow \mathbb{R}$	Powder flow rate [kg/s] at nozzle exit.
f_{eff}	Powder flow rate [kg/s] integrated at the bead.
$\eta \in 0, 1$	Material efficiency ratio f_{eff}/f .
$V(t) : \mathbb{R} \rightarrow \mathbb{R}$	Tool-head or nozzle velocity [mm/s] at time t .
$V(d) : \mathbb{R} \rightarrow \mathbb{R}$	Tool-head or nozzle velocity [mm/s] as a function of the signed distance d (measured in plant view along the bead) to the corner tip.
P	Laser power [W].
v_c	Tool-head cruise velocity [mm/s].
v_{max}	Maximal tool-head cruise velocity [mm/s].
W	Bead width [mm].
$R = W/2$	Half of the bead width [mm].
ρ	Density of the powder cladding material [kg/m ³].
$M \in \mathbb{R}^4 \times \mathbb{R}^4$	Rigid transformation (rotation and translation) matrix resulting from the corner registration.
$[\mathbf{X}_w, \mathbf{Y}_w, \mathbf{Z}_w, \mathbf{O}_w]$	World coordinate system. Basis vectors $\{\mathbf{X}_w, \mathbf{Y}_w, \mathbf{Z}_w\}$ and origin $\mathbf{O}_w \in \mathbb{R}^3$.

1 Introduction

1.1 Research target

This manuscript reports the experimental validation of the method in Ref. [1] that minimizes the overfill of metal in trajectory corners in laser metal deposition (LMD) by varying the cruise velocity of the metal dispenser nozzle. In assessing the deviation between experimental vs. predicted metal beads, the usual registration methods bias the appraisal. To avoid such a bias, this manuscript presents a datum-based sequential registration developed by the authors. This registration progressively matches reliable

datums of the LMD (e.g., substrate plane, bead axes, etc.) between the experimental and predicted datasets. The results show that the variable nozzle velocity strategy significantly reduces the metal overfill at corners, thus approximating the ideal LMD beads.

1.2 Context

LMD is a manufacturing method that employs the power of a laser to manufacture medium- to large-scale industrial parts. It is one of the additive manufacturing (AM) technologies with higher potential to be adopted at industrial scale due to its applications in repairing, coating, and manufacturing of high-value parts (Ref. [2]). One of the main challenges in LMD is the construction of sharp corners since they are prone to unwanted material accumulation.

The computational approach recently presented in Ref. [1] minimizes the material overfill at corners in LMD by adjusting the tool-head velocity at the process-planning stage. The present manuscript reports the experimental validation of this computational minimization method for single-layer trajectory corners of angle $\theta \in \{15^\circ, 30^\circ, 45^\circ, 60^\circ, 75^\circ\}$. For each angle, the method in Ref. [1] is used to find the tool-head velocity that minimizes the material overfill. The experiment consists in the deposition of single-layer corners at controlled (as dictated by the method in Ref. [1]) and constant tool-head velocity. The term *controlled velocity* in this manuscript refers to the fact that the nozzle velocity can be adjusted in advance with predefined parameters resulting from the simulations of variable velocities.

The resulting workpieces are optically scanned. The scanned data are aligned using a datum-based sequential registration developed by the authors. The results of the experiments show that the computational minimization method in Ref. [1] successfully produces tool-head velocity profiles that reduce the material overfill in trajectory corners in LMD. Side findings of the experiments show that around 40% of the powder material is wasted. This waste is inherent to the LMD, regardless of the existence or absence of bead corners. This manuscript does not intend to contribute to the prediction of material waste in LMD. The velocity variation strategy assessed in this manuscript will be integrated into the industrial AM process planning system previously reported in Ref. [3].

The remainder of this article is structured as follows: Section 2 reviews the relevant existing literature. Section 3 describes the methods and materials related to the experiment. Section 4 displays and discusses the computational and experimental results. Section 5 concludes the manuscript and suggests potential extensions of the work.

2 Literature review

2.1 Minimization of material overfill in trajectory corners

In the context of LMD, path planning algorithms generate piecewise linear tool-paths. Material overfill occurs at the tool-path corners due to the following facts: (i) the tool-head reduces its velocity in the vicinity of the corner and (ii) there is an overlap (or double deposition) zone which is larger for sharper corners. The proposed solutions in the literature focus on adjusting three process parameters: laser power, powder flow rate, and tool-head velocity.

The approaches in Refs. [1, 4, 5] vary the tool-head velocity in the vicinity of the corner. Reference [4] executes several experimental trials to find adequate levels of smoothing of right-angle (90°) corners. The material overfill is limited because the smoothed corner is traversed at a higher speed. However, the smoothing compromises geometry accuracy. Reference [5] fits a regression model to predict the bead height as a function of the tool-head velocity, laser power, and powder flow rate. This model is used to modify the tool-head velocity to build right-angled corners. The main drawback of both approaches (Refs. [4, 5]) is that they are limited to trial-and-error experimentation for 90° angles. Reference [1] (precursor of the present one) presents a computational approach to minimize material overfill for several corner angles. This method solves a minimization problem to find a tool-head profile that limits material overfill at the corner. The results reported in Ref. [1] are purely computational, and the experimental validation is missing.

Reference [6] presents an online controller to adjust the laser power during trajectory corners deposition. The reported experiments showed the capability of the system to reduce material overfill at corners. However, this approach changes the bead material properties. It also requires a more expensive computer vision hardware and software to sense the melt-pool during the deposition. Reference [7] presents a control system to regulate the material flow rate. The limitation of this method is the large response time of the powder flow systems. This delay impedes the synchronization of the powder rate decrement with the power or tool-head velocity and position near corners.

The problem of material deposition at corners is common in other AM technologies, such as fused filament fabrication. References [8, 9] implement a computational fluid dynamics model to study the effects of corner smoothing, tool-head velocity, and material feed rate in fused filament fabrication. Numerical results show that synchronizing the feed rate with the tool-head velocity reduces the defects around the corner. However, current hardware limitations hinder the application of this approach in LMD.

2.2 Registration for dimensional inspection

The main techniques for nondestructive dimensional inspection in AM are contact-measurement machines, X-ray computer tomography (XCT), and 3D scanning (Ref. [10]).

References [11] and [12] use contact-measurement machines to assess the geometrical accuracy in parts produced by powder bed fusion and fused filament fabrication, respectively. Contact-measurement machines are the most accurate devices for dimensional inspection in parts manufactured by subtractive methods. However, the surface irregularities in the parts produced via AM disturb the measurements of these machines.

XCT is used in Ref. [13] to measure the porosity and in Ref. [14] to evaluate the internal features in AM-manufactured parts. However, the scanning time of XCT is very high (Ref. [13]). In addition, the voxel format of the XCT method requires additional processing to deliver surface measurement readings.

3D scanning is advantageous because it (i) provides detailed information of the workpiece surface, (ii) offers short data gathering time, and (iii) avoids having contact with the workpiece (Ref. [10]). Reference [15] uses structured-light scanning to examine the surface roughness and thickness distribution in flat pieces built via Wire-and-Arc AM. Reference [16] uses 3D scanning to estimate the volume and the surface roughness of thin plate-based structures also manufactured with Wire-and-Arc AM. Ref. [17] uses structured-light scanning to analyze the accuracy of dental models fabricated via several AM techniques such as, digital light processing, multi-jet printing, and stereolithography. Reference [18] applies 3D laser scanning to reverse-engineer a metal impeller.

For the analysis of dimensional accuracy, the data acquired via 3D scanning must be registered (i.e., aligned) with a reference coordinate system. The standard registration approaches (e.g., iterative closest point (ICP) and feature identification) statistically minimize the distance between the scanned data and a reference (target) model.

The ICP method iteratively applies rigid transformations over the scanned data. These rigid transformations minimize the overall distance between the scanned data and the target model (Ref. [19]). The feature identification method in Ref. [20] processes some particular entities (features) of the workpiece (e.g., planes, spheres, and cones). In this method, an experienced user selects the geometrical features to register between the scanned data and the target model. An overall distance minimization is then applied to simultaneously align all the selected features.

Both conventional and additive manufacturing employ distance-based registration. For example, Ref. [21] uses ICP to measure the deviation of workpieces built via fused

filament fabrication, while Ref. [22] uses ICP for in-line dimensional inspection of warm forged workpieces. However, for the purpose of this work, overall distance-based registration methods cannot be used. The reason is that, when several datums are to be extracted from a point cloud sample, the overall registration moves the sampled points to an equidistant position to all the datums simultaneously. This even-handed approach dramatically biases the sampled data thus disabling any subsequent conclusions about deviation of individual features. In particular, in the scenario of LMD bead overfills, the assessment of a specific *corner* feature would be impossible. In particular, overall registrations would impede the evaluation of the strategy in Ref. [1] to minimize material overfill of bead corners in LMD.

2.3 Bead topography models

Existing literature shows two main trends in bead geometry modeling. In the first strategy, the bead cross section is approximated by a predefined function. References [23, 24] study the ability of parabolic, sinusoidal, and elliptical profiles to model the bead cross section in LMD. Reference [23] considers only single-track deposition. Reference [24] considers multi-track and multi-layer deposition. In both studies (Refs. [23, 24]), the parabolic profile provides the best fit with respect to experimental data. Refs. [25, 26] use parabolic cross-section profile in the simulation of 2D finite element thermal [26] and thermo-fluid [25] models. Reference [27] develops an analytical model to measure the laser power attenuation due to the interaction with the metal powder particles and uses an elliptical cross section. All the previous approaches only model the bead cross section.

They do not address the spatial evolution of the bead geometry under instantaneous changes in the tool-head velocity or material flow rate.

In the second strategy, the distribution of the delivered material on the substrate surface governs the bead geometry. This approach links the bead geometry with instantaneous variations in the tool-head velocity and powder flow rate. Reference [28] concludes that, for coaxial nozzles, the powder on the substrate surface follows a Gaussian distribution. Reference [29] shows that the Gaussian distribution induces good approximations at the bead centerline but not at the sides of the bead cross section. References [30, 31] use the Gaussian profile in the 3D finite element simulation of a thermo-fluid model. The model is used to estimate the evolution of the temperature of the melt-pool and the bead geometry.

As a conclusion, the literature survey indicates that, with the current LMD hardware, the tool-head velocity is a popular mean to diminish overfill in LMD bead corners. However, most of the works that attempt to tailor the tool-head velocity are based on trial-and-error experimentation, which is costly in time and materials. Reference [1], a precursor of the present manuscript, reports a computational approach to adjust the tool-head velocity to reduce the material overfill at corners in LMD.

Table 1 summarizes the existing approaches to limit material overfill in LMD trajectory corners.

The present work focuses on the experimental validation of the method presented in Ref. [1]. The experiment consists in the deposition of single-layer corners with angles $\theta \in \{15^\circ, 30^\circ, 45^\circ, 60^\circ, 75^\circ\}$ built with and without using the tool-head velocity variation in Ref. [1]. It must be remarked that such a validation entails the development

Table 1 Summary of the approaches to limit LMD-corner material overfill

Reference	Tuning variable	Studied angle(s)	Advantages	Disadvantages
Ref. [1]	Tool-head velocity	30°, 60°, 90°	<ul style="list-style-type: none"> • Avoids trial-and-error experimentation 	<ul style="list-style-type: none"> • No experimental validation • Single-layer deposition
Ref. [4]	Tool-head velocity	90°	<ul style="list-style-type: none"> • Multi-layer deposition: 50 layers, 25 mm height 	<ul style="list-style-type: none"> • Test only with 90° angle • Corner smoothing • Trial-and-error experimentation
Ref. [5]	Tool-head velocity	90°	<ul style="list-style-type: none"> • Multi-layer deposition: 70 layers, 11.5 mm height 	<ul style="list-style-type: none"> • Test only with 90° angle • Trial-and-error experimentation
Ref. [6]	Laser power	30°	<ul style="list-style-type: none"> • Fast response time of laser power control hardware 	<ul style="list-style-type: none"> • Single-layer deposition • Requires specialized vision hardware • Test only with 30° angle • Changes bead material properties
Ref. [7]	Powder feed rate	90°	<ul style="list-style-type: none"> • Significant reduction of overfill 	<ul style="list-style-type: none"> • Slow response time of the powder rate controller • Single-layer deposition • Test only with 90° angle
This work	Tool-head velocity	15°, 30°, 45°, 60°, 75°	<ul style="list-style-type: none"> • Avoids trial-and-error experimentation • Several angles studied 	<ul style="list-style-type: none"> • Single-layer deposition • May lead to underfill

and application of a datum-based sequential registration of LMD samples for dimensional inspection.

This manuscript does not intend to predict the portion of the metal powder that does not integrate into the bead. Notice that the powder loss occurs independently of the existence or absence of trajectory corners. Powder loss and bead overflow are both present at LMD trajectory corners. This manuscript addresses only the minimization of corner bead overflow.

3 Methodology

This manuscript reports the experimental validation of the computational method presented in Ref. [1]. Figure 1 shows the procedure followed in this work to assess the deposition of single-layer corners of angles $\theta \in \{15^\circ, 30^\circ, 45^\circ, 60^\circ, 75^\circ\}$. For each corner angle, four results are generated:

1. Corner predicted by simulating the deposition with constant nozzle velocity.
2. Corner predicted by simulating the deposition with variable nozzle velocity (Ref. [1]).
3. Corner physically built with constant nozzle velocity.

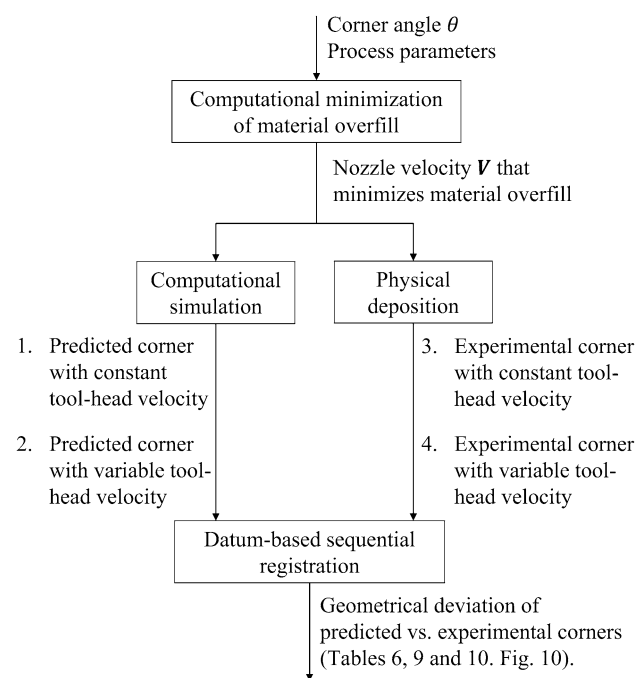


Fig. 1 Prediction vs. experiment assessment. Minimization of bead corner overflow by using variable tool-head velocity (follow up from Ref. [1])

4. Corner physically built with the same nozzle velocity as in item (2) above (variable nozzle velocity provided by the method in Ref. [1]).

Observe that datasets (1), (2), (3), and (4) must be expressed in the same coordinate system in order to permit comparison. This conversion is called *registration*, and it is implemented via a rigid transformation \mathbf{M} . \mathbf{M} is synthesized as the most plausible function that matches specific datums or features in those datasets.

The following sections discuss in detail how the predicted and the experimental corners are generated.

3.1 Material overflow in trajectory corners in LMD

In LMD of corners, the following circumstances are present to compound metal overflow:

1. Geometrical overlap: Fig. 2 shows that material is redundantly deposited in the intersection region around the corner. Unwanted material accumulation in this overlapping region increases with sharper corner angles.
2. Tool-head deceleration: The tool-head must decelerate to draw the corner. Since the powder feed rate remains basically constant, this deceleration concentrates more material in the vicinity of the corner.
3. Hardware limitations: Current hardware does not offer real-time variation of the powder flow rate. Although the material feed rate can be adjusted, the response of the feed system is slow, rendering a basically constant rate (Refs. [5, 6, 32]).
4. Software limitations: Current software for process planning in AM does not consider material overflow at corners during the generation of the nozzle trajectory.

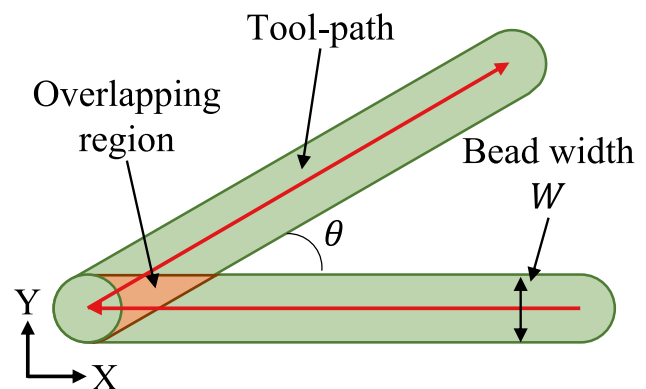


Fig. 2 Plant view of the overlapping region in the vicinity of the corner

3.2 Geometry deposition simulator

This manuscript follows the procedure in Ref. [1] to simulate the deposited geometry in the LMD process. A description of this procedure follows.

Let the planar curve $\mathbf{C}(u) = [C_x(u), C_y(u)]^T, 0 \leq u \leq 1$, be the tool-head path (see Fig. 3). The function $I(x, y, t)$ denotes the powder concentration [kg/(mm² s)] at the substrate surface where the nozzle is depositing the powder. The function I describes variable powder feed rate [kg/s] and tool-head velocity [mm/s]. In this manuscript (as in Ref. [1]), I follows a Gaussian distribution:

$$I(x, y, t) = \frac{2f(t)}{\pi R^2} \exp\left(-\frac{2\left((x - p_x(t))^2 + (y - p_y(t))^2\right)}{R^2}\right) \quad (1)$$

where $\mathbf{p}(t) = [p_x(t), p_y(t)] \in \mathbf{C}$ is the nozzle position, $f(t)$ [kg/s] is the powder flow rate and R [mm] is half of the bead width W [mm].

As an example of the physical meaning of the function I , assume the tool-head is at $\mathbf{p} = [0, 0]$ and it remains static. Also let the bead width be $W = 2$ mm ($R = 1$ mm) and the powder flow rate f be constant. The mass M [kg] deposited on a region $D \subset \mathbb{R}^2$ on the substrate surface is:

$$M = \int_0^t \int_D I(x, y, t) dx dy dt = \frac{2f\Delta t}{\pi} \int_D e^{-2(x^2+y^2)} dx dy \quad (2)$$

where Δt [s] is the time span. The total mass delivered by the nozzle is $M_T = f \Delta t$.

Consider the two circular regions D_1 and D_2 on the substrate surface in Eqs. (3) and (4). The center of D_1 is at the same position as the tool-head. The center of D_2 is 0.8 mm away from the tool-head position. D_1 and D_2 have the same area.)

$$D_1 = \{(x, y) : x^2 + y^2 \leq 0.1^2\} \quad (3)$$

$$D_2 = \{(x, y) : (x - 0.8)^2 + y^2 \leq 0.1^2\} \quad (4)$$

Recalling Eq. (3), the mass deposited on D_1 is $M_1 \approx 0.02M_T$. The mass deposited on D_2 is $M_2 \approx 0.006M_T$. This result shows that, assuming a Gaussian I , the powder concentration is larger at the center point of the laser.

3.2.1 Computational simulation

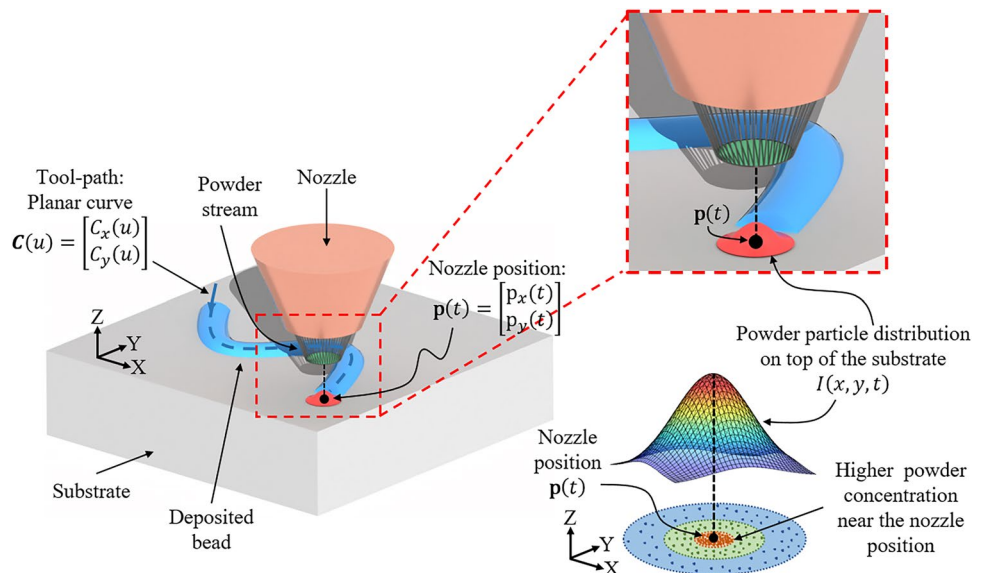
Equation (1) implies that the bead height H at time t , with material density ρ [kg/m³], is:

$$H(x, y, t) = \frac{1}{\rho} \int_0^t I(x, y, \xi) d\xi \quad (5)$$

In order to numerically estimate the bead height H in Eq. (5), the substrate surface is discretized into a rectangular grid (Fig. 4) with vertices (x_i, y_j) . The tool-path curve \mathbf{C} is approximated by the piecewise linear curve $\mathbf{C}^{PL} = [\mathbf{c}_0, \mathbf{c}_1, \dots, \mathbf{c}_N], \mathbf{c}_k \in \mathbf{C}$. The tool-head velocity and the powder flow rate at $\mathbf{c}_k \in \mathbf{C}^{PL}$ are v_k and f_k , respectively.

Let t_k be the instant at which the nozzle is at \mathbf{c}_k . The height H_{ij} at the grid vertex (x_i, y_j) is approximated as in Ref. [1]:

Fig. 3 Geometric simulation of material deposition. The function $I(x, y, t)$ represents the powder concentration [kg/(mm² s)] at the substrate surface



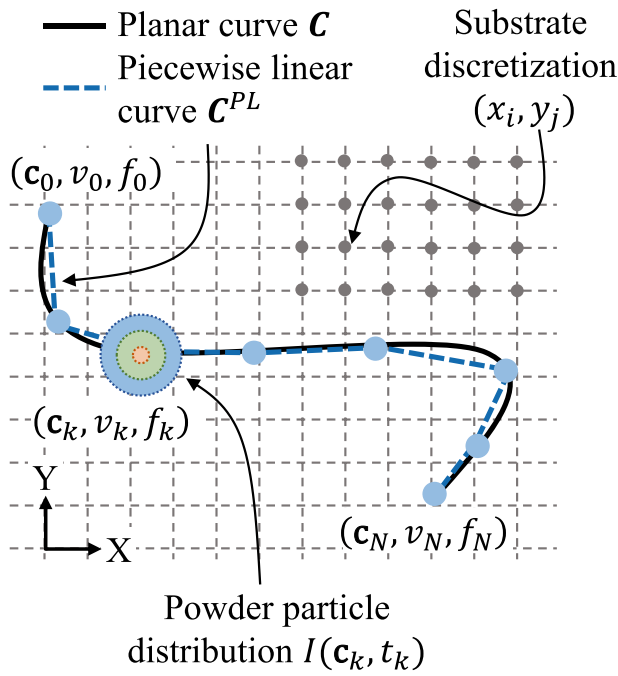


Fig. 4 Piecewise linear approximation of the tool-path. Voxel discretization of the substrate surface. The tool-path discretization is not constrained to the grid vertices

$$H_{ij} = H(x_i, y_j) = \frac{1}{\rho} \sum_{k=1}^N \int_{t_{k-1}}^{t_k} I(x_i, y_i, \xi) d\xi \tag{6}$$

The integral in Eq. (6) is solved using numerical integration.

3.3 Minimization of material overfill at corners in LMD

The present work follows Ref. [1] to minimize the metal overfill at trajectory corners in LMD. This optimization procedure finds the tool-head velocity function $V(t)$ that minimizes the material overfill at the corner.

Reference [1] defines an ideal bead corner topography with no overfill. In it, the corner exit trajectory is defined as a rotation of the entry one. This rotation by the corner angle θ pivots at the corner tip.

Equation (7) (Ref. [1]) computes the bead height of an infinite linear trajectory along the X -axis at steady conditions. v_c is the tool-head velocity [mm/s], and f is the powder flow rate [kg/s].

$$H_0(x, y) = \int_{-\infty}^{\infty} I(x, y, t) dt = \frac{\sqrt{2}f}{\rho\sqrt{\pi}Rv_c} \exp\left(\frac{-2y^2}{R^2}\right). \tag{7}$$

Table 2 Experimental setup. Parameters used in the experiments

Parameter	Value
Material	Stellite 6
Density	$\rho = 8400 \text{ kg/m}^3$
Nozzle cruising velocity	$v_c = 6.67 \text{ mm/s}$
Powder flow rate	$f = 0.12 \text{ g/s}$
Laser power	$P = 1200 \text{ W}$
Bead width	$W = 2R = 2.6 \text{ mm}$
Maximal velocity	$v_{\max} = 2v_c = 13.33 \text{ mm/s}$

The ideal corner for the angle θ , H_G^θ , is built by joining H_0 and its corresponding θ rotation. Figure (5) depicts the ideal corner H_G^θ for $\theta = 30^\circ$ for the process parameters in Table 2.

Equations (9) and (10) pose the optimization problem presented in Ref. [1]. The problem is stated for a substrate surface discretized into a rectangular grid. N_{row} and N_{col} denote the number of rows and columns of the grid. The tuning variable, $V(t)$, is the tool-head velocity function that, for a given angle θ , produces the corner most similar to the ideal corner. The function $e(\mathbf{x})$ in Eq. (10) (Ref. [1]) measures the discrepancy between the ideal corner and the corner achieved with the tuning tool-head velocity V .

find $V(t)$

to minimize $E(V) =$

$$\frac{1}{N_{\text{row}} \cdot N_{\text{col}}} \sum_{i=0}^{N_{\text{col}}} \sum_{j=0}^{N_{\text{row}}} e(x_i, y_j)^2 \tag{8}$$

subject to $0 < V(t) \leq v_{\max}$;

with

$$e(\mathbf{x}) = \begin{cases} |H(\mathbf{x}) - H_G^\theta(\mathbf{x})|, & \text{if } H(\mathbf{x}) < H_G^\theta(\mathbf{x}), \\ & \text{i.e. underfill} \\ 0, & \text{if } H_G^\theta(\mathbf{x}) \leq H(\mathbf{x}) \leq \max(H_G^\theta), \\ & \text{i.e. permissible overfill} \\ H(\mathbf{x}) - \max(H_G^\theta), & \text{if } H(\mathbf{x}) > \max(H_G^\theta), \\ & \text{i.e. overfill} \end{cases} \tag{9}$$

In Eq. (10), $\max(H_G^\theta) = \frac{\sqrt{2}f}{\rho\sqrt{\pi}Rv_c}$ is the maximum height of the ideal corner H_G^θ .

The present work (implemented in MATLAB) uses an exhaustive search to approximate solutions for this optimization problem. Table 3 reports the parameters used in the numerical optimization. The corner entry and exit trajectories, bead topography and velocity V are assumed to be reflections of each other with respect to the plane that bisects the corner (Fig. 5). Moreover, it is assumed that V is a piecewise linear (w.r.t. time) function with four stages.

Table 3 Parameters used in the numerical optimization

Parameter	Value
Optimization method	Exhaustive search
Length of the corner segment	20 mm
Voxel size	0.01 mm
Size of trajectory discretization	0.01 mm
Software	MATLAB

3.4 Materials for the experiments and the 3D scanning

The corner deposition experiments were executed with an *IPG Photonics YLS-6000* high-power fiber laser. The laser beam diameter was 2.5 mm. The optical head was placed in a 3-linear-axis machine. The metal powder was deposited through a coaxial nozzle with Nitrogen as carrier gas. The powder material used was *Stellite 6*, and the substrate was *S355* carbon steel. The powder flow rate, tool-head velocity, and laser power are listed in Table 2.

The deposited corners were scanned with the *Gocator 3210* structured-light scanner. The maximum accuracy of the scanner is 35 μm. The scanner light source is a blue LED emitted at wavelength 465 nm. To adequately capture the details of the workpieces, the scanner was integrated with the *Universal Robots UR10* 6-axis robot arm. Several captures of the workpieces were taken at different poses of the robot. The captures were then consolidated in the same coordinate system to obtain the corresponding 3D mesh of the workpiece.

3.5 Registration of the experimental corners

By definition, an overall standard registration would seek to minimize the distances between the predicted and the experimental plate—bead—corner data. This fact would bias the assessment of the effectiveness of the overfill minimization algorithm. Because of this reason, the present work uses

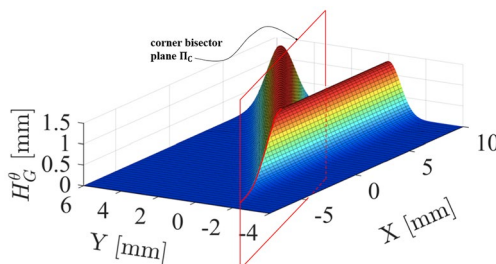


Fig. 5 Ideal corner H_G^θ for $\theta = 30^\circ$ (Eq. (7)) and corner bisector plane Π_C . Process parameters in Table 2

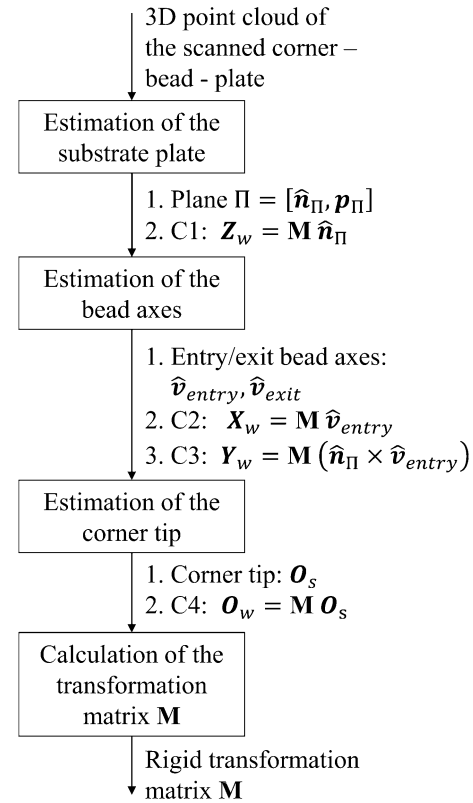


Fig. 6 Registration of the 3D point cloud of the experimental corner. Steps of the proposed datum-based sequential registration

instead a local probing datum-based sequential registration (Fig. 6), implemented in MATLAB, that avoids such a bias.

3.5.1 Problem statement

Given the 3D scanned data (point cloud) of the corner, $S_{\text{sample}} \subset \mathbb{R}^3$, one must find the rigid transformation

$$\mathbf{M} = \begin{bmatrix} \mathbf{R} & \mathbf{T} \\ \mathbf{0} & 1 \end{bmatrix}; \quad \mathbf{R} \in \text{SO}(3); \quad \mathbf{T} \in \mathbb{R}^3; \quad (10)$$

from the local coordinate system to the world coordinate system $[X_w, Y_w, Z_w, O_w]$, as shown in Fig. 7. The matrix \mathbf{M} is different for each scanned corner.

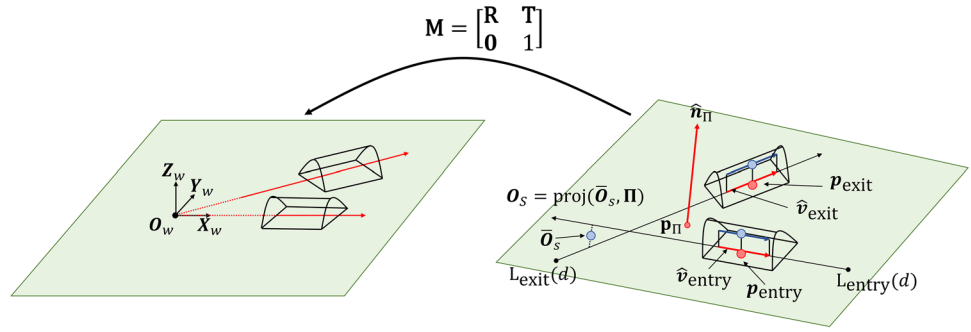
3.5.2 Estimation of the substrate plate

The 3D point cloud S_{sample} is segmented into four subsets:

$$S_{\text{sample}} = S_{\text{plate}} \cup S_{\text{entry}} \cup S_{\text{exit}} \cup S_{\text{rest}}. \quad (11)$$

S_{plate} contains the points on the substrate plate. S_{entry} and S_{exit} contain the points on the steady-state regions of the entry and exit beads. S_{rest} contains all the other points.

Fig. 7 Registration of the scanned data with the world coordinate system. Estimation of the plane of the substrate plate surface and the lines of the bead axes



The substrate plate surface is represented by a plane $\Pi = (\hat{n}_\Pi, \mathbf{p}_\Pi)$. As usual, \hat{n}_Π = plate normal vector, \mathbf{p}_Π = any point on the plane. \hat{n}_Π is the direction of least variance of the point sample and is determined via principal component analysis. \mathbf{p}_Π is estimated as the center of gravity of S_{plate} (Eq. (12)):

$$\mathbf{p}_\Pi = \text{CG}(S_{\text{plate}}). \tag{12}$$

The normal vector \hat{n}_Π sets the first constraint $C1$ needed to find \mathbf{M} :

$$C1 : \mathbf{Z}_w = \mathbf{M} \hat{n}_\Pi. \tag{13}$$

3.5.3 Estimation of the bead axes

Let $L_{\text{entry}} \subset \Pi$ be the line defining the axis of the entry bead:

$$L_{\text{entry}}(d) = \mathbf{p}_{\text{entry}} + d \hat{\mathbf{v}}_{\text{entry}}, \quad d \in \mathbb{R}. \tag{14}$$

The definitions of $\hat{\mathbf{v}}_{\text{entry}}$ and $\mathbf{p}_{\text{entry}}$ follow. Let $\mathbf{v}_{\text{entry}}^*$ be the direction of maximum variability of the points in S_{entry} . This direction is estimated via principal component analysis. The direction vector of L_{entry} , $\hat{\mathbf{v}}_{\text{entry}}$, is the projection of $\mathbf{v}_{\text{entry}}^*$ onto Π :

$$\hat{\mathbf{v}}_{\text{entry}} = \text{proj}(\mathbf{v}_{\text{entry}}^*, \Pi). \tag{15}$$

$\mathbf{p}_{\text{entry}}$ can be estimated as the projection of the CG of S_{entry} onto Π :

$$\mathbf{p}_{\text{entry}} = \text{proj}(\text{CG}(S_{\text{entry}}), \Pi). \tag{16}$$

An analogous procedure is used to find the axis of the exit bead $L_{\text{exit}} \subset \Pi$. Figure 7 shows a graphical representation of the entities involved in this process.

The direction vector of L_{entry} sets the second constraint $C2$ needed to find \mathbf{M} :

$$C2 : \mathbf{X}_w = \mathbf{M} \hat{\mathbf{v}}_{\text{entry}} \tag{17}$$

Since \mathbf{M} represents a rigid transformation, the following constraint, $C3$, arises as a consequence of $C1$ and $C2$:

$$C3 : \mathbf{Y}_w = \mathbf{M} (\hat{n}_\Pi \times \hat{\mathbf{v}}_{\text{entry}}) \tag{18}$$

$C1$, $C2$, and $C3$ determine the $\text{SO}(3)$ vector triad of the coordinate system for the scanned data S_{sample} .

3.5.4 Estimation of the corner tip

The corner tip $\mathbf{O}_s \in \Pi$ is estimated as the intersection between L_{entry} and L_{exit} . \mathbf{O}_s is computed as per Eq. (19):

$$\mathbf{O}_s = \text{proj}(\bar{\mathbf{O}}_s, \Pi) \tag{19}$$

where $\bar{\mathbf{O}}_s$ is the midpoint of the shortest segment that joins L_{entry} and L_{exit} . The final constraint $C4$ needed to compute \mathbf{M} is:

$$C4 : \mathbf{O}_w = \mathbf{M} \mathbf{O}_s \tag{20}$$

Recalling constraints $C1$, $C2$, $C3$, and $C4$, the following linear equation is obtained, with \mathbf{M} as the unknown variable:

$$\begin{bmatrix} \mathbf{Z}_w & \mathbf{X}_w & \mathbf{Y}_w & \mathbf{O}_w \\ 0 & 0 & 0 & 1 \end{bmatrix} = \mathbf{M} \begin{bmatrix} \hat{n}_\Pi & \hat{\mathbf{v}}_{\text{entry}} & \hat{n}_\Pi \times \hat{\mathbf{v}}_{\text{entry}} & \mathbf{O}_s \\ 0 & 0 & 0 & 1 \end{bmatrix} \tag{21}$$

The rigid transformation matrix \mathbf{M} is then calculated as:

$$\mathbf{M} = \begin{bmatrix} \mathbf{Z}_w & \mathbf{X}_w & \mathbf{Y}_w & \mathbf{O}_w \\ 0 & 0 & 0 & 1 \end{bmatrix} \begin{bmatrix} \hat{n}_\Pi & \hat{\mathbf{v}}_{\text{entry}} & \hat{n}_\Pi \times \hat{\mathbf{v}}_{\text{entry}} & \mathbf{O}_s \\ 0 & 0 & 0 & 1 \end{bmatrix}^{-1} \tag{22}$$

Notice that with the implemented method, the upper left (3×3) sub-matrix of \mathbf{M} (i.e., \mathbf{R} in Eq. (10)) is indeed special orthogonal $\text{SO}(3)$.

4 Results

4.1 Computational results

4.1.1 Tool-head velocity profiles

The optimization approach in Sect. 3.3 is used to find tool-head velocity functions that locally minimize the overfill in corners. Computer runs were executed for angles $\theta \in \{15^\circ, 30^\circ, 45^\circ, 60^\circ, 75^\circ\}$.

Figure 8 shows, for each angle, the obtained velocity profile V as function of the signed distance d (measured in plant view along the bead) to the corner tip [mm]. As expected, (i) the velocity increases in the vicinity of the corner tip ($d = 0$) in all cases, and (ii) the velocity increment occurs sooner for smaller angles.

4.1.2 Predicted corners with constant and variable tool-head velocity

Table 4 shows the corners predicted by the geometrical simulator with variable (Fig. 8) and constant tool-head velocity. Table 4 shows significant material overfill at the corners simulated with constant tool-head velocity. The metal overfill is larger for sharper corners ($\theta \in \{15^\circ, 30^\circ\}$). As a result of the corner overfill minimization, the corners with variable tool-head velocity have a more uniform material distribution along the whole trajectory.

4.2 Experimental validation

Table 5 presents the experimental corners resulting from constant and variable tool-head velocity. Table 6 shows the registered scanned data corresponding to the physical corners depicted in Table 5. The comparisons in Table 6 demonstrate that the application of tool-head velocity variation significantly reduces material overfill at the corners.

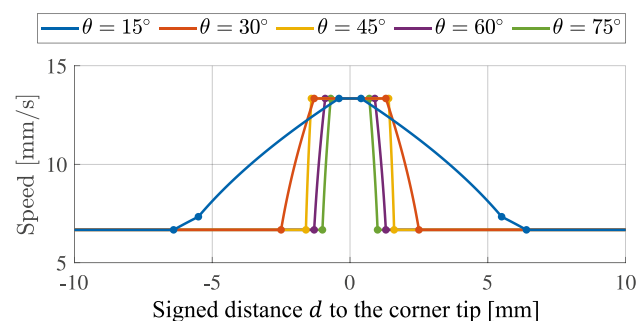


Fig. 8 Tool-head velocity profiles obtained via numerical optimization for $\theta \in \{15^\circ, 30^\circ, 45^\circ, 60^\circ, 75^\circ\}$. Process parameters in Table 2. For entry stage, $d \leq 0$. For exit stage, $d \geq 0$

The height of the corners deposited with variable tool-head velocity is more uniform than the height of the corners built with constant velocity, such as previously observed in the simulated corners.

Table 7 compares the bead height in the overfill zone for the corners resulting from constant and variable tool-head velocity. The average height of the 10 registered datasets at the steady-state region of the entry bead is 0.68 mm. Figure 9 shows the bead height deviation in the overfill zone for the experimental corners resulting from constant and variable tool-head velocity.

Constant tool-head velocity (i) the average bead height in the overfill zone is, as expected, above the reference value (0.68 mm) and (ii) except for $\theta = 45^\circ$, the height deviation w.r.t. the reference value is above 30%. These two facts show that the material overfill at the corner is noticeable when the tool-head velocity is kept constant.

Variable tool-head velocity The bead height deviation nears 10% (except for $\theta = 45^\circ$). It is a significant reduction when compared against the constant tool-head velocity case. The average height in the overfill zone is below the reference value for all the studied angles. It shows that the present approach tends to generate material underfill at the corner. This aspect is particularly apparent for $\theta = 45^\circ$, where the height deficit of the corner with variable tool-head velocity (27%) is higher than for the corner with constant tool-head velocity (17%).

4.3 Comparison of the predicted vs. experimental corners

Table 8 reports the volume of the predicted and experimental corners. The volume of the predicted corners is larger than the volume of the experimental corners. The predicted corners are simulated with the nominal powder flow rate f with the assumption that all the powder material is indeed melted and becomes part of the bead. However, it does not occur in the real LMD process, where an amount of the powder material is wasted (independently from corner existence). The effective powder flow rate f_{eff} , which models the amount of powder that effectively becomes part of the bead is:

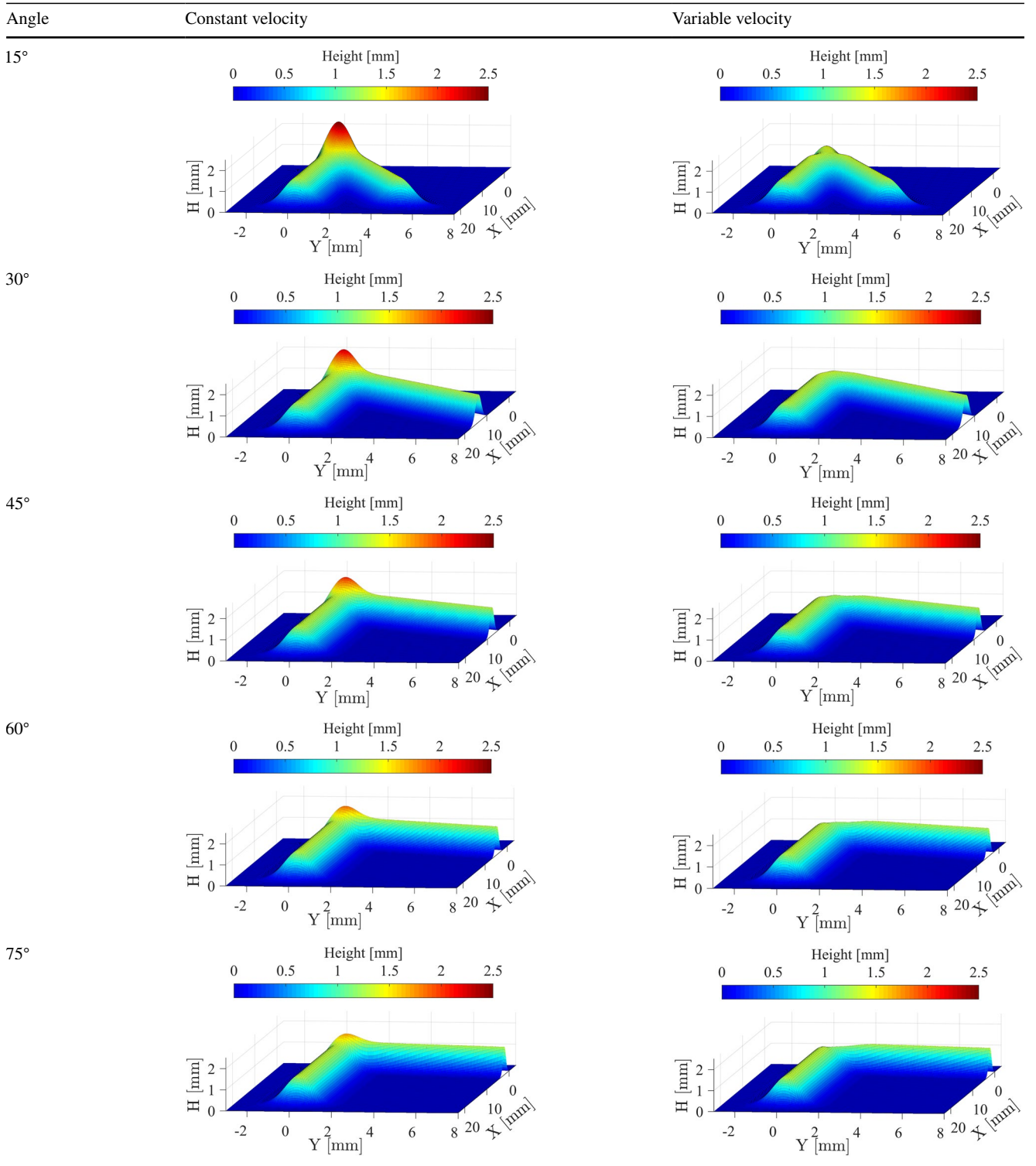
$$f_{\text{eff}} = \eta * f, \quad (\eta \in [0, 1]) \quad (23)$$

where $\eta \in [0, 1]$ is the material efficiency factor.

The value of η was approximated as the average ratio of the volume of the experimental vs. the predicted corners reported in Table 8. The obtained value was $\eta \approx 0.59$. This value shows that, on average, 41% of the powder is wasted in the deposition of the 10 corners.

The predicted model for volume estimation in both constant and variable velocity differs from the measured volume, mainly due to material waste in the process (still difficult to adjust in the theoretical model). But a good

Table 4 Predicted bead geometry by the voxel-based simulator. Comparison of the corners simulated with constant and variable tool-head velocity


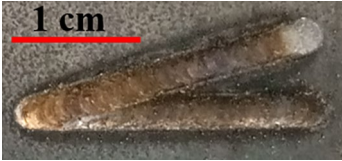
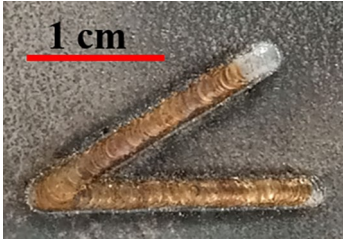
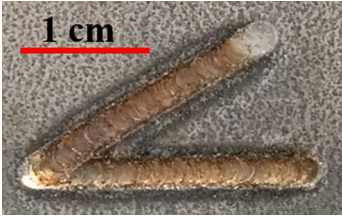
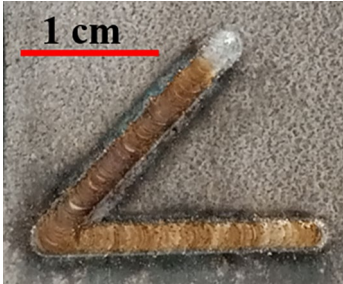
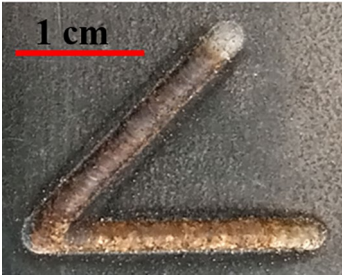
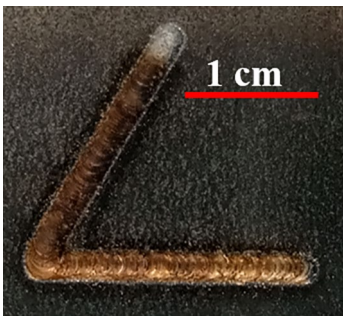

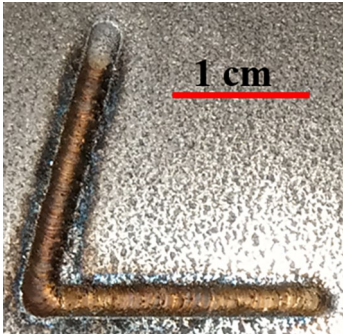



experimental result is that the variable velocity approach indeed reduces sensibly the measured overfill at the corners, and that this reduction effect is more pronounced in sharper angles—columns 2 and 4 in Table 8. Thus, for the

sharper angle of 15° the volume reduction is about 16% (43.7 vs. 51.3 mm³).

Tables 9 and 10 compare the bead height trend of the predicted vs. the experimental corners with constant and

Table 5 Experimental datasets. Deposited corners with constant and variable tool-head velocity

Angle	Constant velocity	Variable velocity
15°		
30°		
45°		
60°		
75°		

variable tool-head velocity, respectively. The bead height is compared at the cross section $Y = 0$ because it corresponds to the zone of maximum height in the entry bead. In both Tables 9 and 10, the bead height of the predicted datasets was adjusted with the material efficiency factor $\eta = 0.59$.

Tables 9 and 10 show a good agreement between the predicted and the experimental datasets. In Table 9, the cross-sectional data at $Y = 0$ for the corners with constant tool-head velocity show that the geometrical simulator overestimates the material overfill for the sharpest corners

Table 6 Experimental validation. Columns 1–2: registered scanned data of the physical specimens in Table 5. Column 3: bead height of variable vs. constant tool-head velocity at $Y = 0$

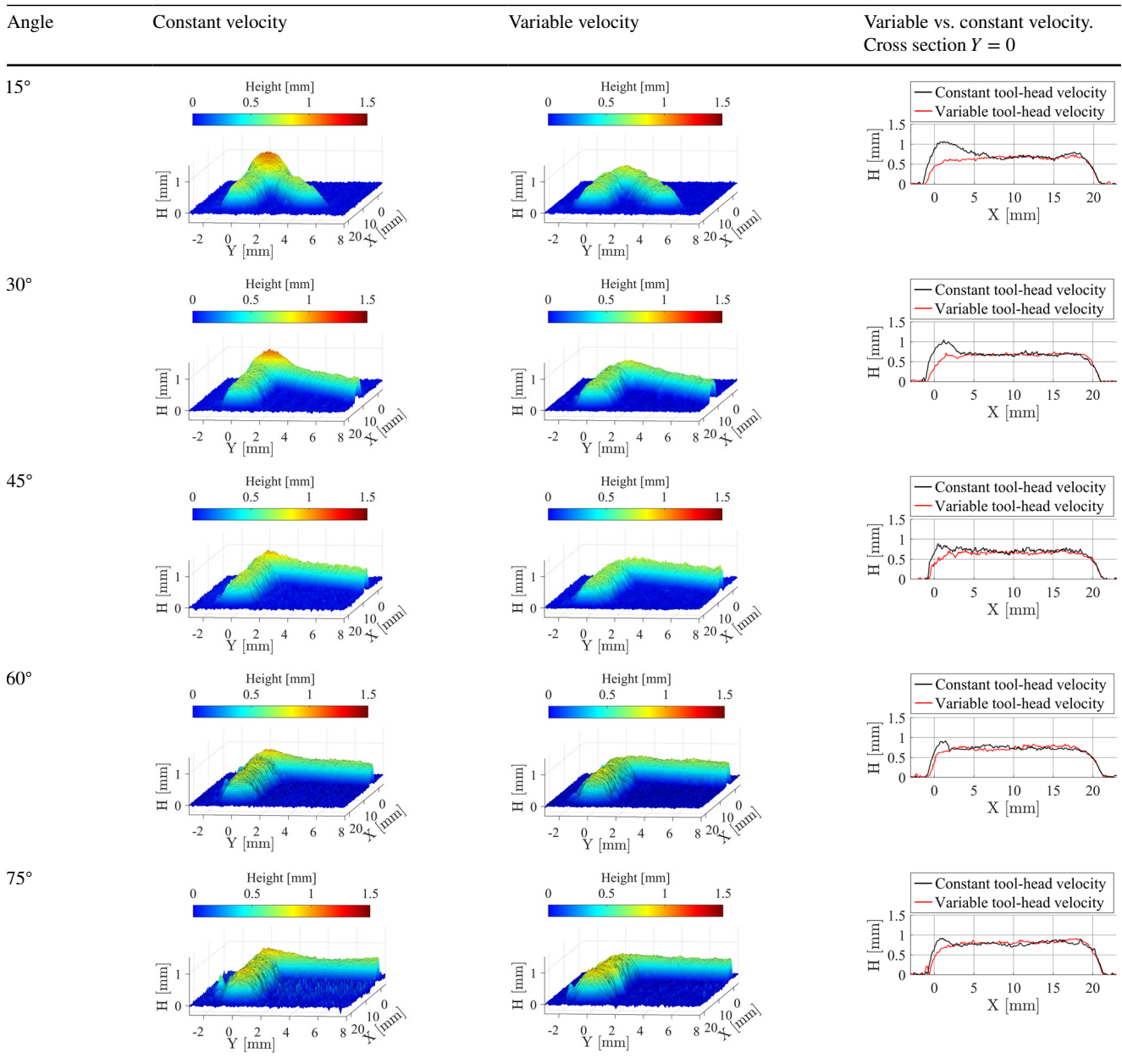


Table 7 Bead height at the corner. Experimental corners. Constant vs. variable tool-head velocity

Angle	Constant velocity		Variable velocity	
	Average height. Overfill zone	Deviation ^a	Average height. Overfill zone	Deviation ^a
$\theta = 15^\circ$	1.1 mm	0.42 mm (61%)	0.6 mm	-0.08 mm (-12%)
$\theta = 30^\circ$	1.0 mm	0.32 mm (47%)	0.6 mm	-0.08 mm (-12%)
$\theta = 45^\circ$	0.8 mm	0.12 mm (17%)	0.5 mm	-0.18 mm (-27%)
$\theta = 60^\circ$	0.9 mm	0.22 mm (32%)	0.6 mm	-0.08 mm (-12%)
$\theta = 75^\circ$	0.9 mm	0.22 mm (32%)	0.6 mm	-0.08 mm (-12%)

^aMeasured w.r.t. the average bead height in the steady zones: 0.68 mm

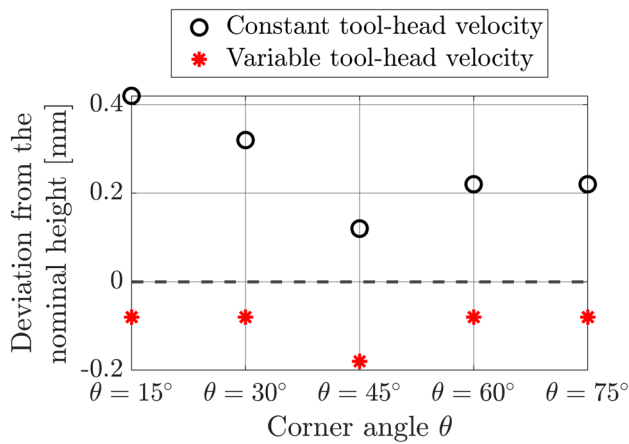


Fig. 9 Experimental corners. Constant vs. variable tool-head velocity. Bead height deviation (Table 7) in the overfill zone

($\theta \in \{15^\circ, 30^\circ, 45^\circ\}$). In the other cases, $\theta \in \{60^\circ, 75^\circ\}$, the approximation of the overfill is correct. For the corners with variable tool-head velocity, Table 10 shows that the predicted corners provide valid estimations of the shape of the experimental corners in the cross section $Y = 0$.

Figure 10 presents the corner of angle $\theta = 30^\circ$ built with variable velocity. The predicted corner in Fig. 10a does not consider material loss, i.e., the material efficiency factor is $\eta = 1$. In Fig. 10a, the predicted corner is always above the experimental corner along the whole trajectory, not only at the corner.

Figure 10b compares the predicted vs. the experimental datasets considering the material loss for the simulation of the predicted corner. This figure supports the previous findings in Table 10, which shows that the geometrical simulator estimates the deposited bead when the effective powder efficiency is known ($\eta = 0.59$).

The previous results show the capacity of the voxel-based simulator to approximate the topography of the bead in LMD trajectory corners and to optimize it for a given set of LMD settings. It is worth mentioning that the material efficiency does not affect the optimization process. The same optimal tool-head velocity profiles are obtained for different values of material efficiency $\eta \in (0, 1]$. On the other hand,

the material efficiency η (usually known to the process engineer) is required to generate accurate predictions of the bead height with the voxel-based simulator.

4.4 Similarities and differences with other approaches

The LMD process settings (e.g., materials, tool-head velocity, laser power) for Refs. [1, 4–7] differ from one reference to the other. The hardware used is also diverse. It is therefore unfeasible to establish numerical comparisons between these works. Hence, this section qualitatively compares this work and the other approaches in Table 1 to limit overfill in LMD trajectory corners.

- Tuning process variable:** Tool-head velocity (Refs. [1, 4, 5]) prevails over the powder feed rate (Ref. [7]) and the laser power (Ref. [6]) as tuning variable. The main reasons are that (i) the response time of the kinematic system is faster than the one of the powder flux system, (ii) additional hardware is not required to modify the tool-head velocity and (iii) material waste additionally weakens the powder feed rate as a tuning variable.
- Trial-and-error vs. computational approaches:** Trial-and-error approaches (Refs. [4, 5]) are costly in time and materials and, therefore, few angles are studied. Computational approaches (e.g., this work and Ref. [1]) reduce experimentation costs and allow the study of several corner angles. In addition, computational approaches can simulate different conditions (e.g., corner angle or process parameters) without adding considerable costs. An advantage (at the present time) of the trial-and-error approaches in Refs. [4, 5] is that they admit multi-layer experiments.
- Corner smoothing:** This approach (Ref. [4]) rounds a 90-degree corner, lowers the tool-head velocity and variates the power delivered to the laser, thus depositing more or less material. The corner is rounded by affecting the *G502* instruction of the G-code and the *e* precision parameter (intervening the CNC controller). Ref. [4] does not present conclusions regarding the use of laser power as a tuning variable. The approach of the present

Table 8 Volume of the predicted and experimental corners

Angle	Constant velocity		Variable velocity	
	Predicted corner	Experimental corner	Predicted corner	Experimental corner
$\theta = 15^\circ$	85.7 mm ³	51.3 mm ³	76.9 mm ³	43.7 mm ³
$\theta = 30^\circ$	85.7 mm ³	49.5 mm ³	81.2 mm ³	45.0 mm ³
$\theta = 45^\circ$	85.7 mm ³	49.3 mm ³	82.4 mm ³	46.3 mm ³
$\theta = 60^\circ$	85.7 mm ³	51.9 mm ³	83.2 mm ³	49.7 mm ³
$\theta = 75^\circ$	85.7 mm ³	55.1 mm ³	83.7 mm ³	51.4 mm ³

Table 9 Corners built with constant tool-head velocity. Predicted ($\eta = 0.59$) vs. experimental datasets

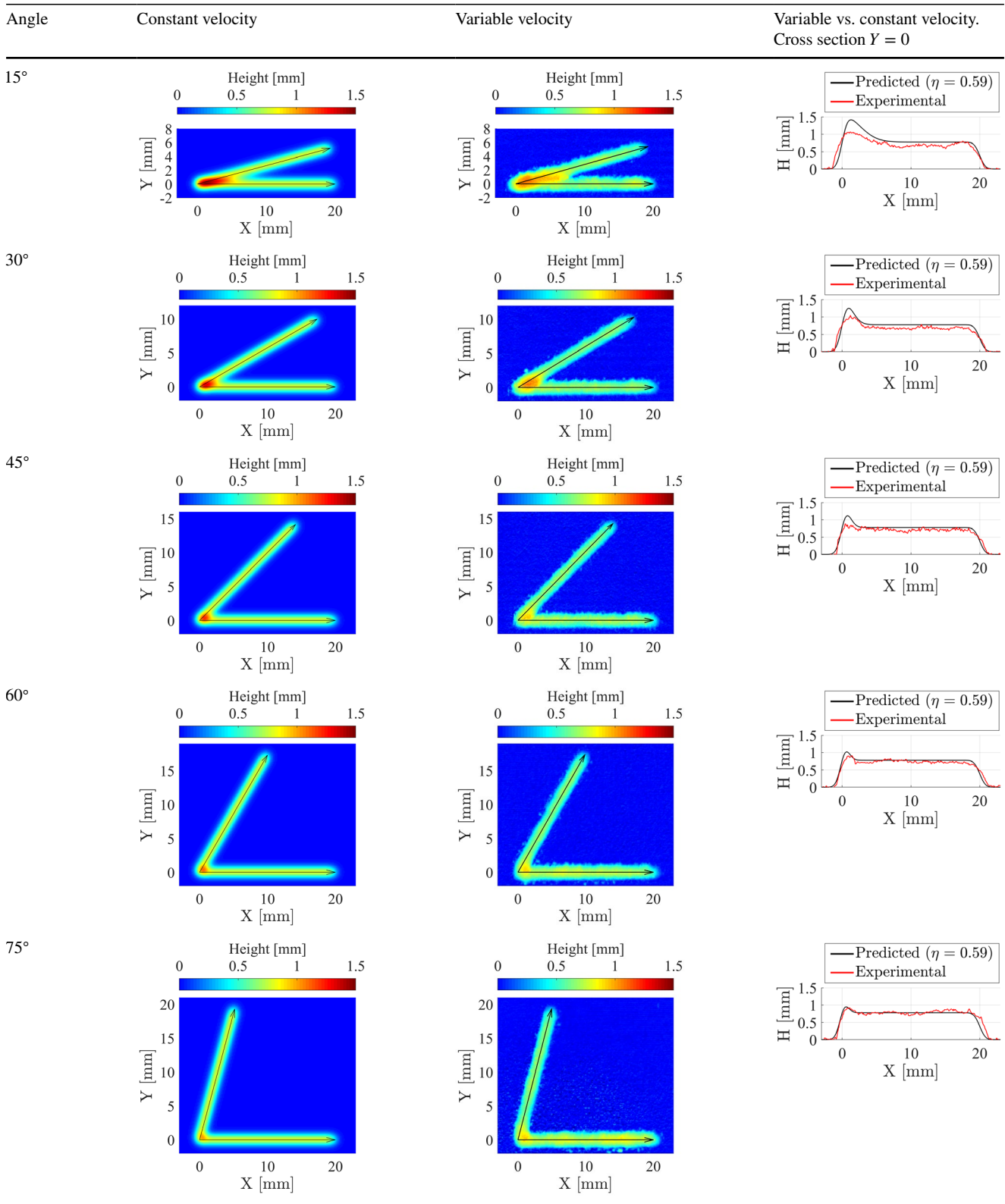
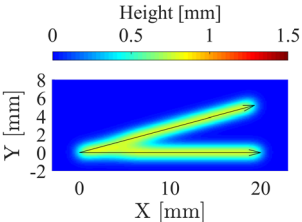
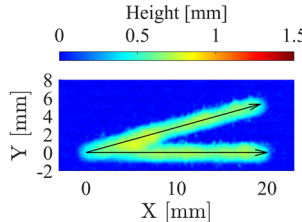
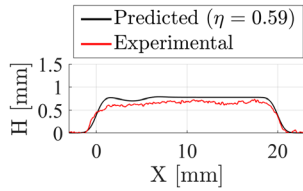
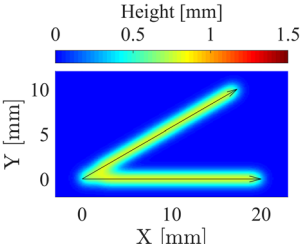
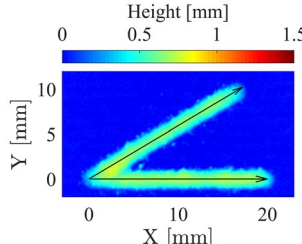
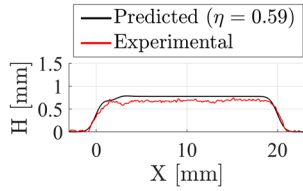
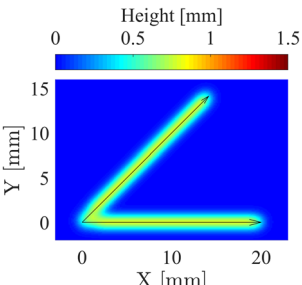
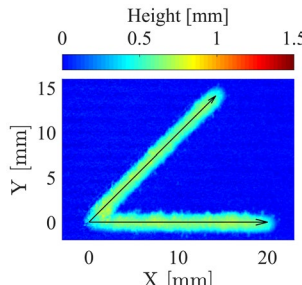
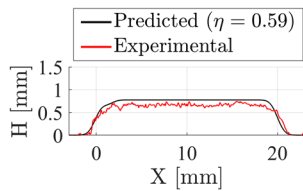
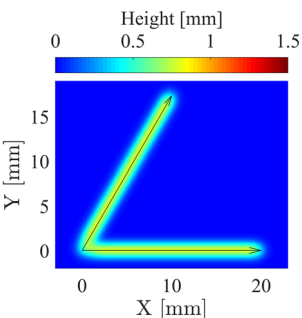
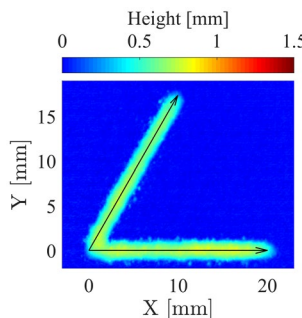
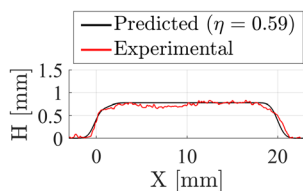
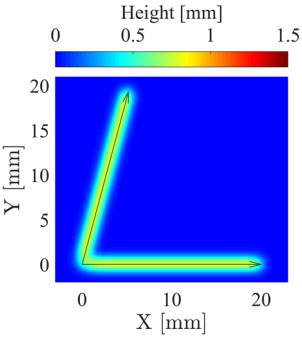
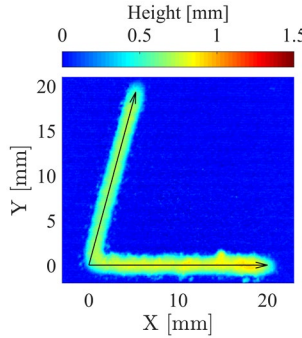
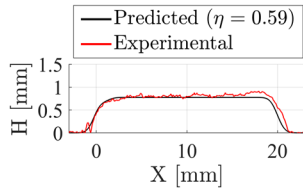


Table 10 Corners built with variable tool-head velocity. Predicted ($\eta = 0.59$) vs. experimental datasets

Angle	Constant velocity	Variable velocity	Variable vs. constant velocity. Cross section $Y = 0$
15°			
30°			
45°			
60°			
75°			

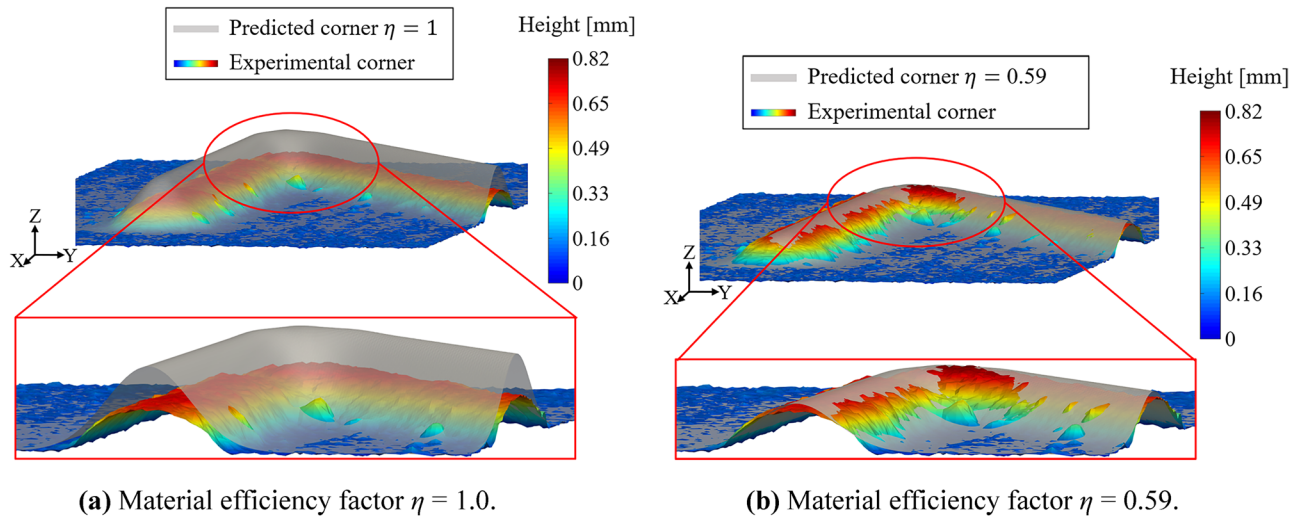


Fig. 10 Predicted vs. experimental datasets. Corners built with variable velocity. Corner angle $\theta = 30^\circ$

manuscript is not to change the path geometry and therefore is not a competitor for Ref. [4].

5 Conclusions

This manuscript presents the experimental validation of the computational approach in Ref. [1] to use variable tool-head velocity in order to limit unintentional material accumulation in trajectory corners in laser metal deposition (LMD). To validate the method in Ref. [1], single-layer corners with angles $\theta \in \{15^\circ, 30^\circ, 45^\circ, 60^\circ, 75^\circ\}$ are built with and without tool-head velocity variation. The results of the experiments show that:

1. The studied tool-head velocity variation effectively limits material overfill for the trajectory corners with angles $\theta \in \{15^\circ, 30^\circ, 60^\circ, 75^\circ\}$. After applying the tool-head velocity variation, the maximum height deviation reduces from 61% to 12% and from 32% to 12% for the angles $\theta = 15^\circ$ and $\theta = 75^\circ$, respectively. This result shows that the benefit of the tool-head velocity strategy is greater for smaller angles.
2. A significant underfill of 27% around the corner tip is observed for $\theta = 45^\circ$ when the tool-head velocity variation is applied.
3. Metal powder waste is an important aspect to consider in LMD. In the experiments reported in this manuscript, a considerable amount (near 40%) of metal powder dispensed by the nozzle is wasted. This material loss is present along the whole trajectory, and it is independent of the presence of corners in the trajectory.

4. The manufacturing engineer plans the LMD process, using the nominal material feed [kg/s], the nozzle trajectories, material efficiency η , etc. Observe that the material efficiency for a particular process/machine is generally known to the process engineer and is present regardless of the presence/absence of trajectory corners. The presented strategy for minimizing the metal overfill prescribes velocity profiles at the trajectory corners. When the LMD (with these velocity profiles) is executed, the engineer finds that the corners significantly improve, as compared against the constant velocity counterparts. On the other hand, the *overall* multi-layer deposition progresses according to the process/machine material waste (approx. 40%). As a consequence, the number of layers required to clad the workpiece increases. However, the focus of this manuscript (i.e., the metal overfill minimization at corners) is substantially achieved.

Additional work is necessary over the computational approach to control the effect (2) above. Future work will also be devoted to extending the current overfill minimization strategy to multi-layer situations.

5.1 Context of application

This manuscript reports the extension of the capabilities of process planning in additive manufacturing (Refs. [3, 33]). The manuscript reports the experimental validation of a method to limit unwanted metal overfill. This computational method is to be integrated into a larger LMD planning tool (Ref. [3]).

Author Contributions Diego Montoya-Zapata, Jorge Posada, Aitor Moreno, and Oscar Ruiz-Salguero were involved in the conceptualization; all the authors contributed to the methodology; all the authors contributed to the formal analysis and investigation; Diego Montoya-Zapata, Jorge Posada, Carles Creus, Aitor Moreno, and Oscar Ruiz-Salguero contributed to writing; Oscar Ruiz-Salguero, Jorge Posada, and Aitor Moreno were involved in the supervision; Diego Montoya-Zapata and Aitor Moreno contributed to the software; Diego Montoya-Zapata and Oscar Ruiz-Salguero contributed to the applied computational geometry aspects.

Funding This work has been partially funded by the Basque Government under ELKARTEK program (grants KK-2018/00115 (ADDIS-END) and KK-2018/00071 (LANGILEOK)) and by the INZU Group (Talens Systems and Ikerkune A.I.E.).

Data Availability The data in this study are not available due to industrial confidentiality restrictions.

Code Availability The code in this study is not available due to industrial confidentiality restrictions.

Declarations

Ethics approval Not applicable.

Consent to participate Not applicable.

Consent for publication The authors and their affiliation institutions have given permission to publish this manuscript.

Conflicts of interest The authors declare that they have no conflicts of interest.

References

- Montoya-Zapata D, Creus C, Moreno A, Ortiz I, Alvarez P, Ruiz-Salguero O, Posada J (2021) Computational minimization of over-deposition at corners of trajectories in Laser Metal Deposition. *Manuf Lett* 29:29–33
- Leino M, Pekkarinen J, Soukka R (2016) The role of laser additive manufacturing methods of metals in repair, refurbishment and remanufacturing - enabling circular economy. *Physics Procedia* 83:752–760
- Montoya-Zapata D, Creus C., Ortiz I, Alvarez P, Moreno A, Posada J, Ruiz-Salguero O (2021) Generation of 2.5D deposition strategies for LMD-based additive manufacturing. *Procedia Computer Science* 180:280–289
- Pereira JC, Borovkov H, Zubiri F, Guerra MC, Caminos J (2021) Optimization of thin walls with sharp corners in SS316L and IN718 alloys manufactured with laser metal deposition. *Journal of Manufacturing and Materials Processing* 5(1):5
- Woo Y, Han S, Oh I, Moon Y, Ha W (2019) Control of directed energy deposition process to obtain equal-height rectangular corner. *Int J Precis Eng Manuf* 20(12):2129–2139
- Baraldo S, Vandone A, Valente A, Carpanzano E (2020) Closed-loop control by laser power modulation in direct energy deposition additive manufacturing. In *Proceedings of 5th International Conference on the Industry 4.0 Model for Advanced Manufacturing* L. Wang, V. D. Majstorovic, D. Mourtzis, E. Carpanzano, G. Moroni, and L. M. Galantucci, Eds., Springer International Publishing, pp. 129–143
- Arrizubieta JI, Martínez S, Lamikiz A, Ukar E, Arntz K, Klocke F (2017) Instantaneous powder flux regulation system for laser metal deposition. *J Manuf Process* 29:242–251
- Comminal R, Serdeczny MP, Pedersen DB, Spangenberg J (2018) Numerical modeling of the material deposition and contouring precision in fused deposition modeling. In *Proceedings of the 29th Annual International Solid Freeform Fabrication Symposium: An Additive Manufacturing Conference*, pp. 1855–1864
- Comminal R, Serdeczny MP, Pedersen DB, Spangenberg J (2019) Motion planning and numerical simulation of material deposition at corners in extrusion additive manufacturing. *Addit Manuf* 29:100753
- Charalampous P, Kostavelis I, Tzovaras D (2020) Non-destructive quality control methods in additive manufacturing: a survey. *Rapid Prototyp J* 26(4):777–790
- Rivas Santos VM, Thompson A, Sims-Waterhouse D, Maskery I, Woolliams P, Leach R (2020) Design and characterisation of an additive manufacturing benchmarking artefact following a design-for-metrology approach. *Addit Manuf* 32:100964
- Kacmarcik J, Spahic D, Varda K, Porca E, Zaimovic-Uzunovic N (2018) An investigation of geometrical accuracy of desktop 3D printers using CMM. *IOP Conference Series: Materials Science and Engineering* 393:012085
- Khosravani MR, Reinicke T (2020) On the use of X-ray computed tomography in assessment of 3D-printed components. *J Nondestruct Eval* 39:4
- Thompson A, Maskery I, Leach RK (2016) X-ray computed tomography for additive manufacturing: a review. *Meas Sci Technol* 27(7):072001
- Laghi V, Palermo M, Gasparini G, Girelli VA, Trombetti T (2021) On the influence of the geometrical irregularities in the mechanical response of wire-and-arc additively manufactured planar elements. *Journal of Constructional Steel Research* 178:106490
- Näsström J, Brueckner F, Kaplan AFH (2019) Laser enhancement of wire arc additive manufacturing. *J Laser Appl* 31(2):022307
- Yoo S-Y, Kim S-K, Heo S-J, Koak J-Y, Kim J-G (2021) Dimensional accuracy of dental models for three-unit prostheses fabricated by various 3D printing technologies. *Materials* 14(6):1550
- Kladovasilakis N, Kontodina T, Charalampous P, Kostavelis I, Tzetzis D, Tzovaras D (2021) A case study on 3D scanning, digital repair and rapid metal additive manufacturing of a centrifugal impeller. *IOP Conference Series: Materials Science and Engineering* 1037(1):012018
- Zhu L, Barhak J, Srivatsan V, Katz R (2006) Efficient registration for precision inspection of free-form surfaces. *Int J Adv Manuf Technol* 32(5–6):505–515
- Sánchez JR, Segura Á, Barandiaran I (2017) Fast and accurate mesh registration applied to in-line dimensional inspection processes. *Int J Interact Des Manuf* 12(3):877–887
- Decker N, Wang Y, Huang Q (2020) Efficiently registering scan point clouds of 3D printed parts for shape accuracy assessment and modeling. *J Manuf Syst* 56:587–597
- Mejia-Parra D, Sánchez JR, Ruiz-Salguero O, Alonso M, Izaguirre A, Gil E, Palomar J, Posada J (2019) In-line dimensional inspection of warm-die forged revolution workpieces using 3D mesh reconstruction. *Appl Sci* 9(6):1069
- Caiazza F, Alfieri V (2019) Simulation of laser-assisted directed energy deposition of Aluminum powder: Prediction of geometry and temperature evolution. *Materials* 12(13):2100
- Ocelík V, Nenadl O, Palavra A, De Hosson J (2014) On the geometry of coating layers formed by overlap. *Surf Coat Technol* 242:54–61
- Tian H, Chen X, Yan Z, Zhi X, Yang Q, Yuan Z (2019) Finite-element simulation of melt pool geometry and dilution ratio during laser cladding. *Appl Phys A* 125:7

26. Ya W, Pathiraj B, Liu S (2016) 2D modelling of clad geometry and resulting thermal cycles during laser cladding. *J Mater Process Technol* 230:217–232
27. Zhou S, Dai X, Zheng H (2011) Analytical modeling and experimental investigation of laser induction hybrid rapid cladding for Ni-based WC composite coatings. *Opt Laser Technol* 43(3):613–621
28. Taberero I, Lamikiz A, Ukar E, López de Lacalle L, Angulo C, Urbikain G (2010) Numerical simulation and experimental validation of powder flux distribution in coaxial laser cladding. *J Mater Process Technol* 210(15):2125–2134
29. El Cheikh H, Courant B, Branchu S, Hascoët J-Y, Guillén R (2012) Analysis and prediction of single laser tracks geometrical characteristics in coaxial laser cladding process. *Opt Lasers Eng* 50(3):413–422
30. Arrizubieta JI, Lamikiz A, Klocke F, Martínez S, Arntz K, Ukar E (2017) Evaluation of the relevance of melt pool dynamics in laser material deposition process modeling. *Int J Heat Mass Transf* 115:80–91
31. Taberero I, Lamikiz A, Ukar E, Martínez S, Celaya A (2013) Modeling of the geometry built-up by coaxial laser material deposition process. *Int J Adv Manuf Technol* 70(5):843–851
32. Ding Y, Warton J, Kovacevic R (2016) Development of sensing and control system for robotized laser-based direct metal addition system. *Addit Manuf* 10:24–35
33. Mejia D, Moreno A, Arbelaiz A, Posada J, Ruiz-Salguero O, Chopitea R (2017) Accelerated thermal simulation for three-dimensional interactive optimization of computer numeric control sheet metal laser cutting. *J Manuf Sci Eng* 140(3):031006

Publisher's Note Springer Nature remains neutral with regard to jurisdictional claims in published maps and institutional affiliations.